Supplementary Information for Time-Wavelength Multiplexed Photonic Neural Network Accelerator for Distributed Acoustic Sensing Systems

Fuhao Yu,[a,d†] Kangjian Di,[b,c,d†] Wenjun Chen,[b,c,d] Sen Yan,[a,d] Yuanyuan Yao,[a,d] Silin Chen,[b,c,d] Xuping Zhang,[a,d] Yixin Zhang,[a,d,*] Ningmu Zou,[b,c,d,*] and Wei Jiang[a,d*]

[a] *Nanjing University, College of Engineering and Applied Sciences, Key Laboratory of Intelligent Optical Sensing and Manipulation, Ministry of Education, Nanjing, China*

[b] *Nanjing University, School of Integrated Circuits, Suzhou, China*

[c] *Nanjing University, Interdisciplinary Research Center for Future Intelligent Chips (Chip-X), Suzhou, China*

[d] *Nanjing University, Key Laboratory of Optoelectronic Manipulation, Ministry of Education, Nanjing, China*

†*These authors contributed equally to this work*

Supplementary notes S1-S8;

Supplementary figures S1-S22;

Contents

Supplementary notes

S1 The results of Photonics convolution operation

According to the principles of Convolutional Neural Networks (CNNs), feature maps are generated by convolving the input images with convolutional kernels. The kernels slide over the images and compute feature values. Multiple convolutional kernels can produce multiple feature maps, thereby extracting rich information from the images. Therefore, the number of convolutional kernels used in each convolutional layer directly determines the number of feature maps output by that layer [32]. Each kernel is designed to capture specific features, such as edges, textures, or other patterns, while different input images contain different features. Consequently, even with the same convolutional kernel, the resulting feature maps from different images will differ.

In our experiment, we set the number of convolutional layers to 1 and the number of convolutional kernels to 10. This allows each kernel to learn different types of features, enhancing the model's expressive capability. Additionally, using multiple kernels can reduce the risk of overfitting since the model structure remains relatively simple with a moderate number of parameters. This configuration also improves computational efficiency by allowing the parallel generation of feature maps, thereby accelerating the training process. Overall, this approach effectively balances the diversity of feature extraction with model complexity, contributing to improved model performance.

Considering that photonics convolution operations process one-dimensional(1D) data, it is necessary to convert image information into 1D data according to the principles of convolutional kernels and then revert the results of the multiplication operation back into two-dimensional images. In each classification task, the results after one layer of optical convolution are illustrated in Figure S1, which shows the outcomes of convolving 10 different images with 10 different convolutional kernels for each class.

S2 The principle of achieving full connected operation through MZM

The convolutional layer extracts features from the input image and transforms them into high-dimensional feature maps. After undergoing nonlinear activation and pooling processes, these feature maps are flattened into a one-dimensional vector, which serves as the input to the fully connected layer. The core principle of the fully connected layer is to multiply this flattened feature vector by a set of learnable weights. After multiplying the input data with the weights, the resulting vector from the fully connected multiplication is summed up, then, the model obtains an output vector that represents a linear combination. The same set of weights will be multiplied with different feature maps to obtain an output value. Each of output value corresponds to a score for different classes, which can be used to determine which class the input image belongs to. Ultimately, the class associated with the neuron that has the highest score is selected as the classification result [46].

Based on this, the principle of implementing fully connected operations using two modulators primarily relies on the ability of these devices to control the intensity of the input optical signals, thereby enabling multiplication operations on the signals. For the first Mach-Zehnder Modulator (MZM), the relationship between the input optical power P_{in} and the output optical power P_{out} can be expressed as:

$$P_{1out} = P_{1in} \cdot M_1\left(v_{1i}\right)$$

$M_1(v_{1i})$ is the modulation function of the first modulator for the radio frequency (RF) input signal v_{1i}. The modulated optical beam P_{1out} then enters the second modulator, where it undergoes further modulation based on the second RF input signal v_{2i}. At this point, the output optical power can be expressed as:

$$P_{2out} = P_{1out} \cdot M_2\left(v_{2i}\right) = P_{1in} \cdot M_1\left(v_{1i}\right) \cdot M_2\left(v_{2i}\right)$$

where $M_2(v_{2i})$ represents the modulation function of the second modulator. It is noteworthy that both M_1 and M_2 are in the form of cosine functions. This process enables the modulation of the optical signal based on both RF input signals, effectively

performing the desired operations for the fully connected layer.

Since the operating points of the two modulators are at orthogonal points, the outputs near these points exhibit an approximate linear relationship with the RF input signals v_{1i} and v_{2i}, as shown in Figure S2. Thus, this method allows for the multiplication of the two input signals. In the context of the TWM-PNNA system, the first modulator is used to load the flattened 1D data of the feature map into optical path, as shown in Figure S3, while the second modulator is used to load the weight information. The results after the optical fully connected layer are illustrated in Figure S4. Additionally, to ensure that the two RF signals are matched, the two modulators are connected in series, and it is essential to maintain equal lengths for the RF signal connection lines between the two modulators. A phase shifter (Spectrum, S-0140-KFKM) is employed to adjust the phases of the input RF signals to both modulators, ensuring that they are time-aligned.

S3 Noise control of push-pull modulation and single-drive modulation

Regarding modulation chirp and its impact on accuracy, it is indeed necessary to carefully control various noise sources during the experimental process. We compared the eye diagrams of push-pull modulation under driving voltage V_{pp1}=-V_{pp2}=1.5V and single ended modulation driving voltage V_{pp}=3V, and tested their signal-to-noise ratio (SNR) to reflect the influence of noise. The experimental results are shown in Figures S5 and S6. It can be observed from the figures that under the same extinction ratio, the SNRs of push-pull modulation and single-drive modulation are similar, indicating that factors other than noise contribute to the precision. Additionally, the voltage required for push-pull modulation is half that of single-arm modulation, further demonstrating the low-power advantage of push-pull modulation.

S4 Energy efficiency estimation

Another key metric for optical computing, aside from speed, is power consumption. In our proof-of-concept setup, power consumption is primarily attributed to tunable lasers, EDFA, modulator drivers, WSS, and other components. However, since this demonstration relies on discrete devices, it is challenging to fully illustrate the ultimate capabilities of our approach. Thanks to the development of hybrid and monolithic integration techniques [52,53], as well as advancements in related technologies, the functions of the discrete devices used in the experiment can be implemented using integrated chips, which provides the possibility to measure the power consumption of TWM-PNNA systems. Therefore, to address the energy efficiency estimation issue of the TWM-PNNA system, we estimate the energy efficiency of a fully integrated optical TWM-PNNA system based on similar protocols from prior works (refs. [19,20,54]).

According to ref [20], the main sources of power consumption include light sources and optical amplifiers and the high-speed optical-electronic conversion processes in input (modulator) and output (photodetector). Among them, the on-chip pump power required for generating the microcomb can be as low as 98 mW [52] and on-chip SOAs typically consume 390 mW [53]. In addition, the power consumption required for the weighting process can be reduced by using low loss phase change materials [51]. The power consumption on the input side comes from the modulator itself as well as from the drivers, ADCs and DACs, while the energy consumption of photodetection is primarily determined by the TIA. Therefore, the estimated power costs are as follows: 5.36 pJ/sample for the modulator with driver (28 GHz) [47], 2 pJ/conversion for the ADC (8 bits) [48], 2.72 pJ/conversion for the DAC (8 bits) [49] and 1.14 pJ/sample for the TIA (53 GHz) [50].

So, the computing speed of our prototype TWM-PNNA is 1.6 TOPS, with an estimated power consumption of $98 + 390 + (5.36 + 1.14 + 2.72 + 2) \times 20 \times 6 = 1834$ mW (fully connected computation requires an additional five modulators). This results in an energy efficiency of approximately 0.87 TOPS/W. For a TWM-PNNA with a 9×9

kernel matrix and a modulation rate of 50 Gbaud, the computing speed would increase to 2×10×81×50= 81 TOPS, with a corresponding power consumption of 98 + 390 + (5.36 + 1.14 + 2.72 + 2) × 50×6 = 3854 mW (3.854 W). The estimated energy efficiency in this case would be approximately 21.02 TOPS/W.

It is important to note that these power consumption estimates are based on ideal conditions. Despite some challenges with integrated TWM-PNNA, there are still significant advantages in energy efficiency compared to electronic products such as CPUs and GPUs. Further, we compared the performance of the most advanced integrated photon computing architecture and electronic GPU in various aspects, as shown in Table S1. In addition, the optical neuron in the table reflects the scale of the network.

Table S1. Comparison of state-of-the-art integrated photonic computing architecture and electrical GPUs

Source	Data loading rate (Gbaud)	Operations Per Second (TOPs)	Power (W)	Energy Efficiency (Tops/W)	#optical neuron
WDM+PCM [54]	2	0.12	3.33	0.4	20
InP SOA [56]	10	-	-	0.24	44
Photonic neuron [57]	N/A	0.27	3.75	0.07	67
Diffractive cell [58]	1×10^{-5}	2×10^{-3}	0.0175	0.11	260
PPU [20]	17	0.136	0.679	0.2	12
Nvidia Jetson Nano [55]	N/A	0.5	5-10	0.05	N/A
This work	20	1.6	1.83	0.87	1660
This work in theory	50	81	3. 85	21.02	

Based on the table data, we plotted the figure of power versus operations per second under different computing architectures as shown in Fig. S7. In addition, we also provide the following analysis on the performance of TWM-PNNA and electronic chips in terms of latency or time to completion for algorithms (s), cost, physical size, or

reliability:

1. **Latency and Time-to-Completion**:

   When calculating latency, it is necessary to consider the delays in various stages such as input preparation, output detection, gradient update and the length of the physical path, etc. [19, 59]. Our solution uses optical fibers to achieve dispersion delay, so the physical path dominates in latency. The longest fiber we used in the experiment is 7.35 km, and the propagation rate of light in the fiber is 2×10^8 m/s. Therefore, the latency caused by the physical path is approximately 36.8 μs, which is a constant value related to the length of the fiber. The delay caused by modulators and photodetectors is at the ns level [13]. However, by using waveshaper or dispersive fiber (dispersion coefficient -200 ps/km/nm), the length of the optical path used can be significantly shortened, thereby reducing the latency of the system by a factor 10 or more.

2. **Cost and Physical Size:**

   Our system incorporates numerous a number of discrete components (lasers, modulators, EDFAs, WSSs, etc.), which increases the cost and physical size. However, recent advances in hybrid integration [60], bonding [61] and transfer printing [62] of silicon photonics can help reduce the size of the TWM-PNNA via chip-scale integration, significantly reducing cost and physical size.

3. **Reliability:**

   Reliability is more suitable for systems entering the product stage, and requires long-term testing. Our study is in its early research and is not suitable for reliability testing. However, the integration of advanced materials [63], combined with the optimization of CMOS processes [64] and robust packaging technologies [65] can provide some help in improving the reliability and yield of device manufacturing in the future.

S5 Future oriented all-optical DAS event recognition system

Figure S8 illustrates the schematic diagram of a forward-looking, all-optical approach

for processing DAS data. In this envisioned all-optical DAS signal processing system, the fiber plays a dual role, serving both as a sensing element and as an optical delay line for convolution operations. The system is powered by a multi-wavelength NLL, which serves as the light source for the entire architecture. To address the requirements for event recognition in areas of interest, the system integrates optical storage to retain the acquired sensing signals. These stored optical signals are then processed along the optical path, employing an IQ demodulation scheme to extract and unwrap phase information, ultimately recovering complete phase data. Building on this foundation, optical convolution weighting and fully connected operations are performed using a TWM-PNNA-based optical neural network for event classification. This work represents a significant step toward future DAS systems that rely entirely on optical methods, integrating optical storage, delay, demodulation, phase unwrapping, and neural network-based event recognition for unprecedented efficiency and scalability.

S6 Comparison of classification Results

Table S2 presents the accuracy of both test and training sets across various image dimensions, including 16×16, 32×32, 36×36, 64×64, and 128×128. To validate the impact of image resolution on the results, in these control experiments, except for the difference in image resolution, all other parameters remain the same. The table illustrates that a notable drop in accuracy occurs at the 16×16 size, suggesting a considerable loss of image detail. Moreover, the table reveals that the accuracy for 32×32 and 128×128 images is nearly identical, implying that beyond a certain threshold, the size of the image has a negligible effect on accuracy. The specific confusion matrix is shown in Figure S9-S13. Additionally, table S3 examines the classification accuracy of both binary and non-binary images using an electrical neural network across different image dimensions. The results indicate that converting the DAS data image to binary form does not appreciably diminish its accuracy, suggesting that the image's information integrity is preserved post-conversion. The specific confusion matrix is shown in Figure S14-S18.

Table S2. Comparison of classification accuracy for optical and electrical neural network under different sizes.

Input Size	128×128	64×64	36×36	32×32	16×16
Train-electrical	99.29%	99.36%	99.49%	99.22%	94.07%
Test-electrical	98.65%	98.25%	98.11%	98.51%	91.25%
Train-optical	95.69%	95.32%	95.92%	95.42%	91.65%
Test-optical	93.53%	94.89%	94.61%	95.56%	89.77%

Table S3. Comparison of classification accuracy for electrical neural network with/without binary under different sizes.

Input Size	128×128	64×64	36×36	32×32	16×16
Train-electrical-binary	99.29%	99.36%	99.49%	99.22%	94.07%
Test-electrical-binary	98.65%	98.25%	98.11%	98.51%	91.25%
Train-electrical-non-binary	99.76%	99.66%	99.56%	99.49%	95.18%
Test-electrical-non-binary	98.38%	97.98%	98.25%	98.38%	91.65%

S7. Experimental details of the optical computing system

In the specific experiment, the system begins with 4 independent tunable lasers emitting light at 4 wavelengths, spaced by 2 nm, which form the 2×2 convolution kernels. These wavelengths (1546.52 nm, 1548.52 nm, 1550.52 nm and 1552.52 nm, the power of each laser is set to 0 dBm.) are combined into a single beam after passing through a Wavelength Division Multiplexer (WDM). The effectiveness of WDM in enhancing data transmission, system capacity, and signal integrity has been extensively demonstrated in prior studies. The combined beam then enters an optical switch (OSW), outputting from port A of the switch into a Mach-Zehnder modulator (MZM, Fujitsu, FTM7937EZ, bandwidth 30 GHz).

A 36×36 pixel binarized image obtained from the DAS database is flattened into a 1D vector X and encoded into an arbitrary waveform generator (AWG, Tektronix, AWG7000B). The method of data unfold is shown in Fig.S19. The modulator, operating at the quadrature point, encodes this vector into an optical time-domain signal, with

each pixel represented by one bit of the modulated signal. Additionally, the maximum bandwidth of this modulator is 30 GHz. The AWG transmits the signal at 10 G baud, and at this point, vector X is simultaneously modulated onto all 4 wavelengths. The output vector is obtained by detecting the signals in each time slot.

A single-mode fiber (SMF) of a certain length provides progressive delays for each channel to match the baud rate of the data emitted by the AWG, ensuring that the signals on adjacent wavelength channels are time-shifted by the same number of symbol positions. Here, the dispersion coefficient of the single-mode fiber is 17 ps/km/nm, so the required fiber length to achieve a symbol shift is 2.9 km. Next, an EDFA is employed to compensate for the insertion loss of the modulator and the loss of light at different wavelengths after passing through the SMF. The EDFA is set to 5 dBm.

The amplified wavelength channels are then shaped by a wavelength-selective switch (WSS, CoAdna, 50GHz Nx1-1.2), which functions as a combination of WDM and filters. The WSS provides flexible wavelength selection and routing while controlling the attenuation of each wavelength channel. This attenuation represents the weight information applied to each wavelength channel, allowing the weight value W_i to be assigned to wavelength λ_i. Subsequently, the output light enters a high-speed photodetector (PD, Finisar, XPDV21x0, bandwidth 40 GHz), which aggregates the total optical power at each wavelength. Additionally, the WSS can realize different convolution kernels by reconfiguring the routing and attenuation of different wavelength channels.

Finally, the electrical output waveform after the photonic convolution is sampled and digitized by a high-speed oscilloscope (OSC, Tek, DPO75902SX) to obtain the feature map. The optical switch is then adjusted so that the laser light emitted from the lasers enters through port B of the switch. The flattened feature map is also loaded into the optical path through the AWG and MZM. The output light from the modulator passes through the WDM, filtering the laser light so that each output channel contains only one wavelength. Furthermore, each output channel of the WDM connects to an MZM to load different weight parameters, thereby achieving multiplication operations. The output light then enters the PD and is collected by the OSC, completing the addition

operations required for the fully connected layer.

This process demonstrates the system's ability to perform optical convolution and fully connected layer operations efficiently, leveraging advanced optical components and precise parameter control.

S8. Reliability and repeatability of results.

In this study, we primarily focused on evaluating the model's classification performance using Recall, Precision, and F1-score, as these metrics are widely accepted in machine learning for assessing classification effectiveness. The detailed evaluation metrics for recall, precision and F1-score of the Electronic Neural Network Model and TWM-PNNA are presented in Table S4 and Table S5, respectively. Recall measures the model's ability to correctly identify positive class samples and is related to the rows of the confusion matrix, reflecting the model's coverage capability for a specific class. Precision, on the other hand, evaluates the proportion of predicted positive samples that are truly positive and is associated with the columns of the confusion matrix, indicating the accuracy of the model's predictions for a specific class. The F1-score, a harmonic mean of recall and precision, provides a balanced measure of the model's overall performance. These metrics comprehensively reflect the model's performance across various aspects, such as coverage capability, accuracy, and balance, helping to validate the model's robustness and generalization ability. If the experiment maintains high Recall, Precision, and F1-score across different datasets or environments, it indicates that the model possesses high repeatability and reliability. For the TWM-PNNA model in distributed sensing event recognition, performance is strong at higher resolutions (128×128 to 32×32), with recall, precision, and F1-scores consistently exceeding 98% for most classes, such as Recall2, Recall3, and Recall4. However, performance declines at the lower resolution of 16×16, particularly for Recall1 (84.56%) and Precision4 (87.42%), indicating reduced effectiveness in identifying certain events, such as background events, at lower resolutions. While F1-scores remain robust at higher

resolutions (e.g., F1-Score2 at 96.98% for 32×32), they drop significantly at 16×16 (e.g., F1-Score1 at 89.24%). It can be seen while the TWM-PNNA model faces challenges in event recognition at lower resolutions, it performs well at higher resolutions (such as 36×36, which is primarily used in the experiment), demonstrating a certain level of reliability and repeatability.

In addition to these classification metrics, we further assessed the consistency and accuracy of the feature maps generated by optical and electronic computing. Specifically, we computed the Root Mean Square Error (RMSE) and Mean Absolute Percentage Error (MAPE) between the optical and electronic feature maps to quantify their similarity, as shown in Fig. S20 and Fig. S21. It can be seen that the error between the TWM-PNNA and electronic computing feature maps is small, with a maximum RMSE of only 0.0208, indicating that the overall numerical deviation is well-controlled. The maximum MAPE of 7.2577% suggests that some feature points have slightly higher relative errors, but the overall consistency remains good. Furthermore, we analyzed the standard deviation (STD) of classification performance across different tasks in both TWM-PNNA and electronic domains, as shown in Fig. S22. The standard deviation of classification tasks in TWM-PNNA and electrical computing is close, indicating that these errors will not significantly affect the final performance, and the repeatability and reliability of TWM-PNNA results are strong.

Table S4. Evaluation Metrics for the Electronic Neural Network Model.

	128×128	64×64	36×36	32×32	16×16
Accuracy	99.17%	99.11%	99.22%	99.08%	93.51%
Recall1	97.36%	97.08%	97.45%	96.99%	88.74%
Recall2	99.64%	99.76%	99.76%	100.00%	96.17%
Recall3	100.00%	100.00%	100.00%	100.00%	94.61%
Recall4	100.00%	100.00%	100.00%	99.79%	95.91%
Precision1	100.00%	100.00%	100.00%	99.81%	95.45%
Precision2	99.17%	98.94%	99.29%	99.17%	92.08%
Precision3	98.76%	98.76%	99.10%	98.99%	94.61%
Precision4	98.63%	98.63%	98.41%	98.31%	91.65%
F1-Score1	98.66%	98.52%	98.71%	98.38%	91.97%
F1-Score2	99.41%	99.35%	99.53%	99.58%	94.08%

F1-Score3	99.38%	99.38%	99.55%	99.49%	94.61%
F1-Score4	99.31%	99.31%	99.20%	99.04%	93.73%

Table S5. Evaluation Metrics for the TWM-PNNA.

	128×128	64×64	36×36	32×32	16×16
Accuracy	95.26%	95.23%	95.67%	95.45%	91.28%
Recall1	87.07%	86.53%	87.97%	87.61%	84.56%
Recall2	98.77%	99.15%	99.14%	99.01%	94.81%
Recall3	99.29%	99.52%	99.30%	99.18%	94.04%
Recall4	99.09%	99.31%	99.09%	98.98%	94.08%
Precision1	99.22%	99.61%	99.22%	99.32%	94.48%
Precision2	94.68%	95.98%	94.92%	95.04%	90.66%
Precision3	94.94%	93.60%	96.07%	95.06%	92.25%
Precision4	91.75%	91.33%	92.07%	91.97%	87.42%
F1-Score1	92.75%	92.61%	93.26%	93.10%	89.24%
F1-Score2	96.68%	97.54%	96.98%	96.98%	92.69%
F1-Score3	97.07%	96.47%	97.66%	97.07%	93.14%
F1-Score4	95.28%	95.15%	95.45%	95.34%	90.63%

Supplementary references

All references are added in the reference list following the main document.

Supplementary figures

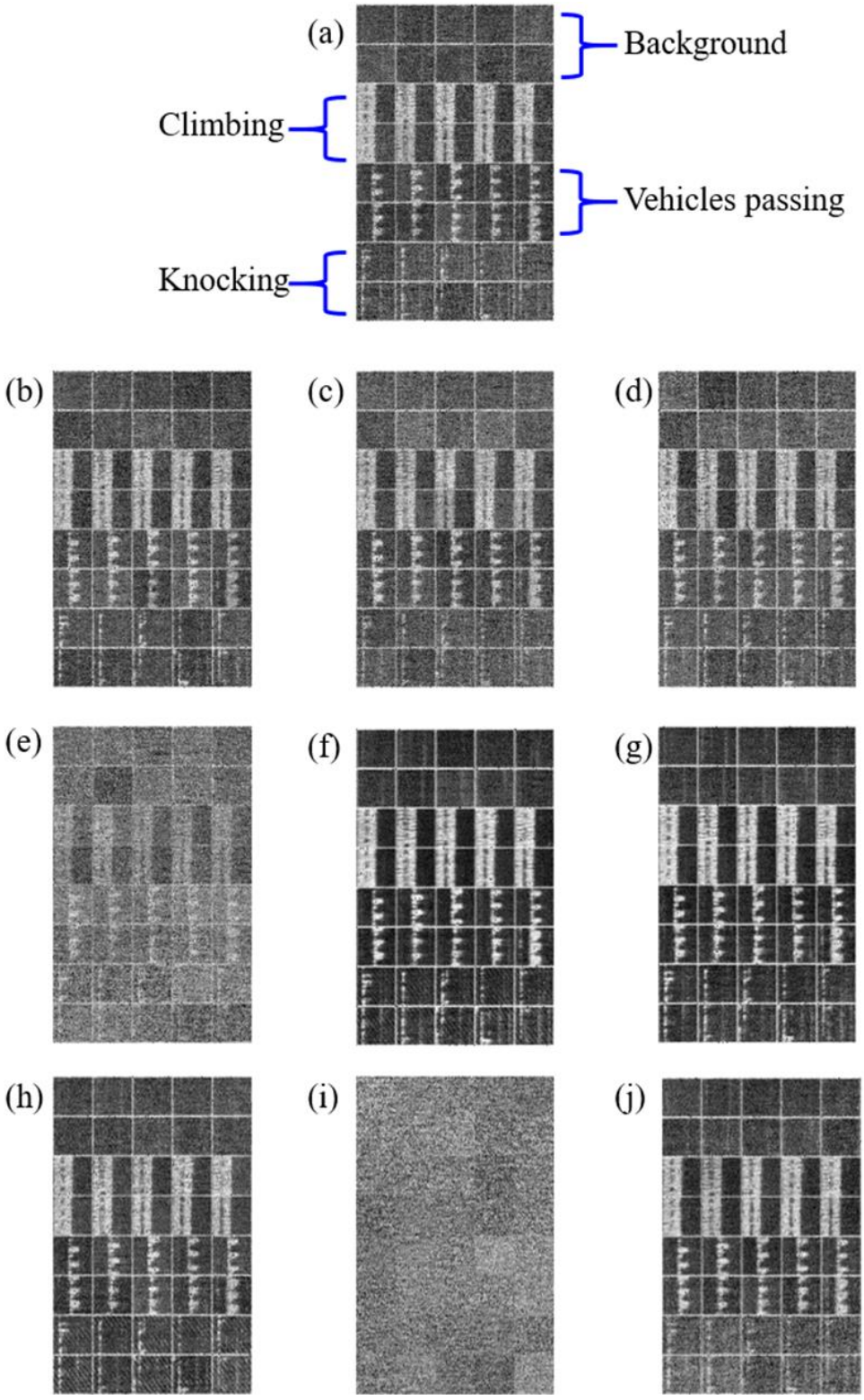

Fig. S1. The results of convolving 10 images from each category with 10 different convolutional kernels. (a~j):kernel1~kernel10.

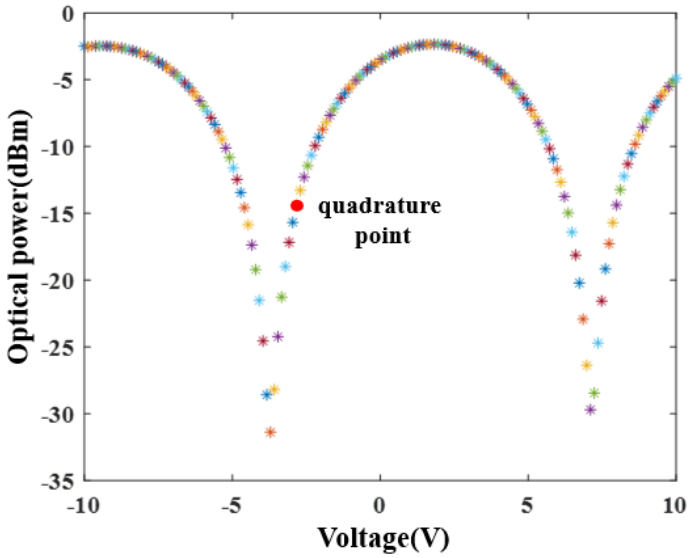

Fig. S2. Measured spectra of the MZM.

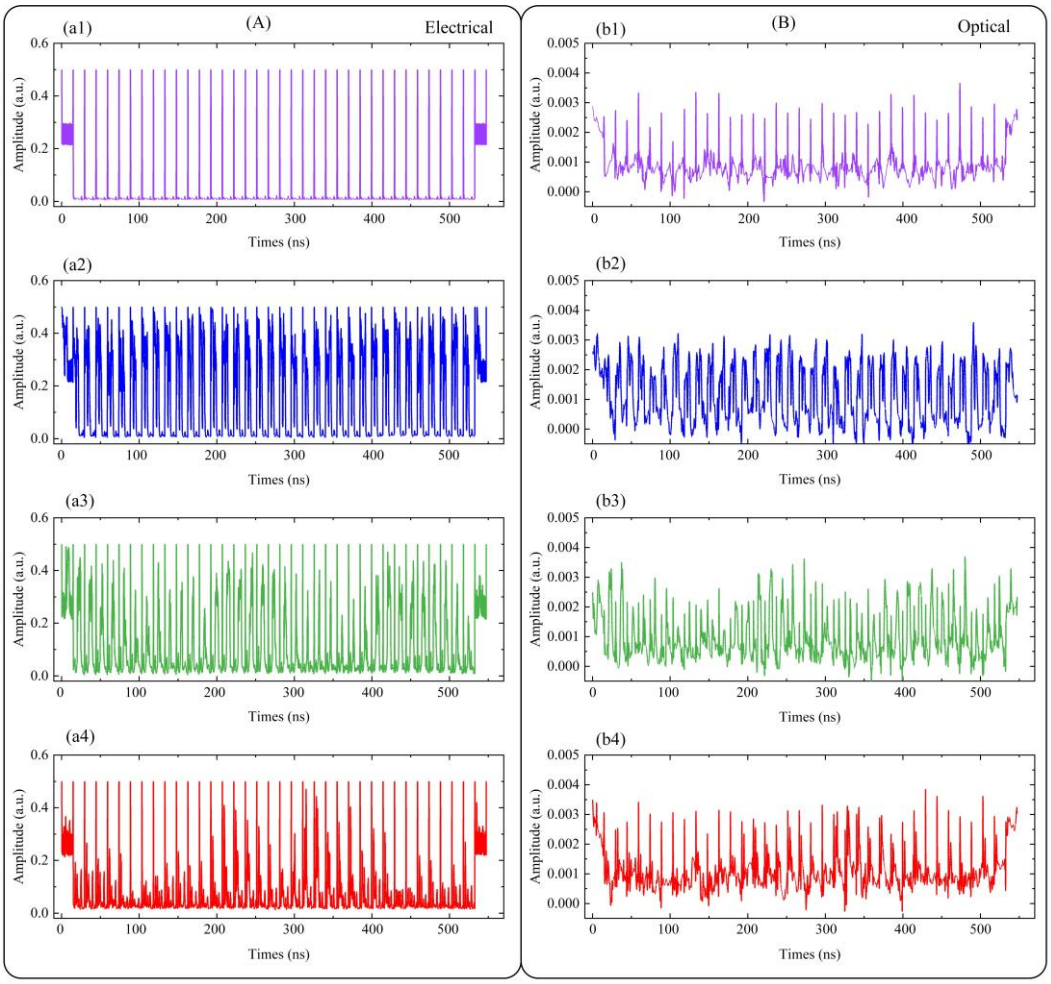

Fig. S3. Flattened 1D Feature Map. (a1-a4): Electrical signal; (b1-b4): Optical signal modulated by the first MZM.

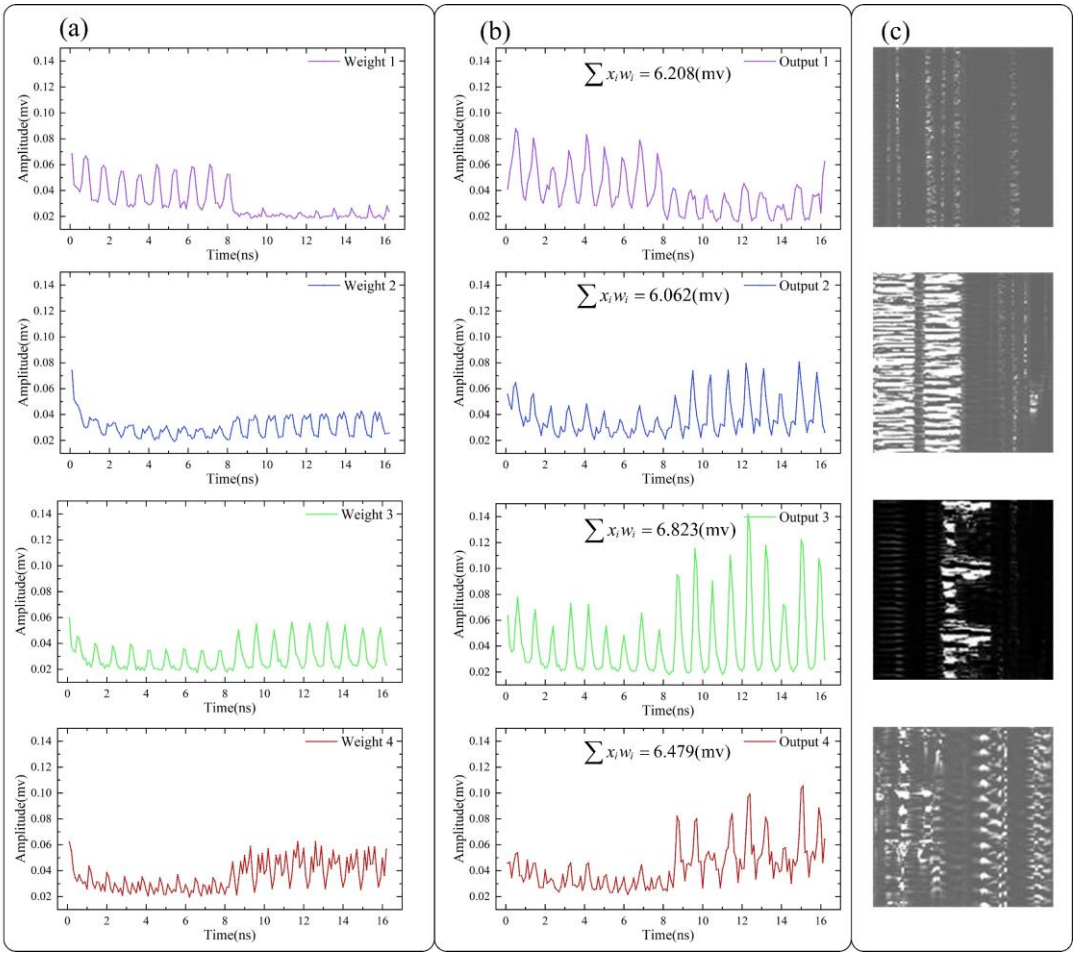

Fig. S4. Results of optical fully connected operation. (a) weights corresponding to each classification event; (b) results of multiplying images by their corresponding weights; (c) classification results of the events

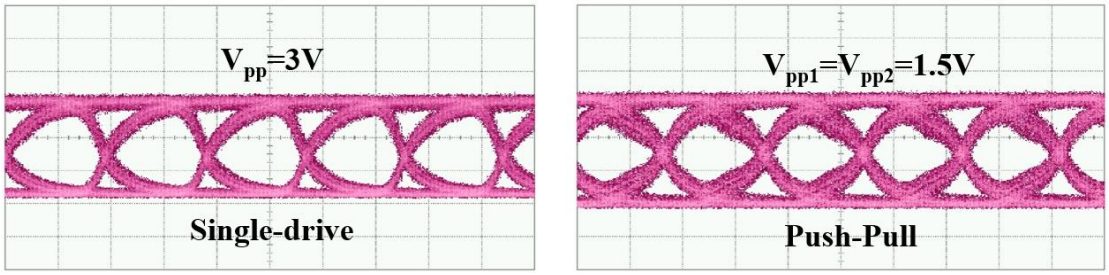

Fig. S5. Eye diagram results of push-pull and single ended modulation in back-to-back situations.

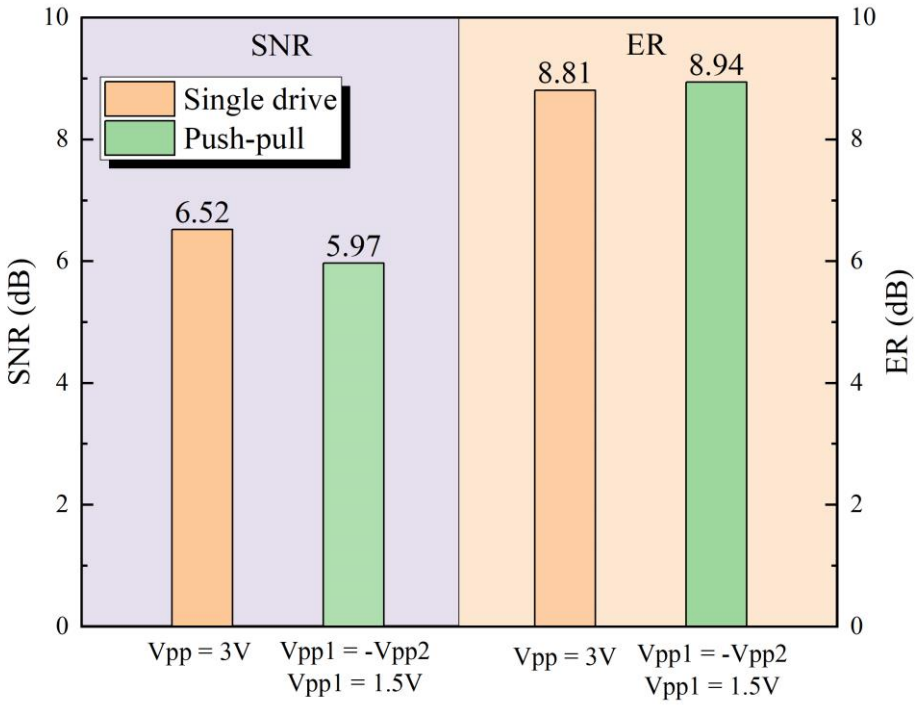

Fig. S6. The ER and SNR results of push-pull and single ended modulation in back-to-back situations.

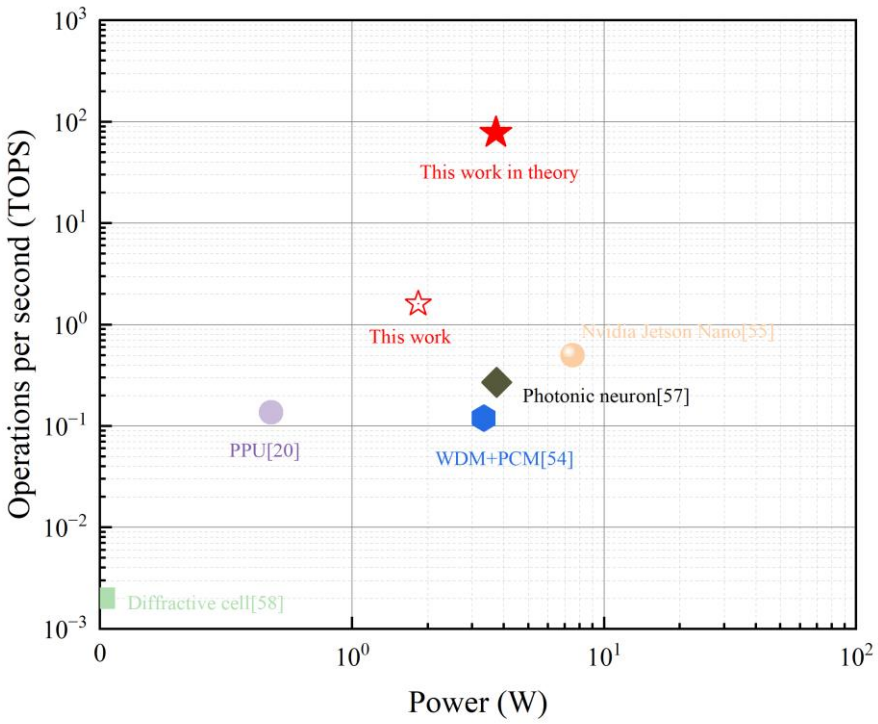

Fig. S7. Schematic diagram of power versus operations per second under different computing architectures.

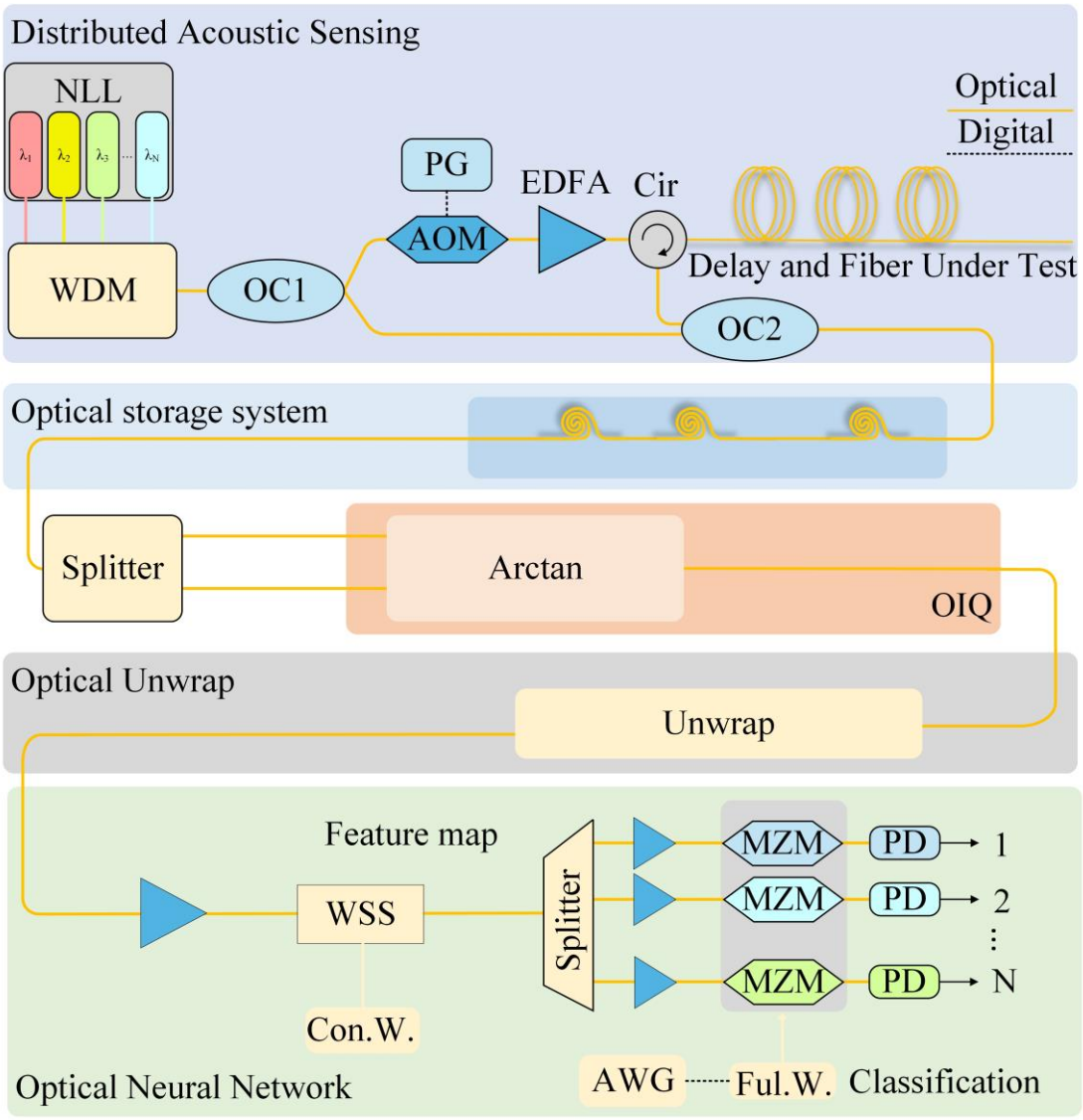

Fig. S8. Schematic diagram of the principle of all-optical processing of DAS data, including the DAS sensing section, optical storage section, optical demodulation section, and optical neural network data processing section.

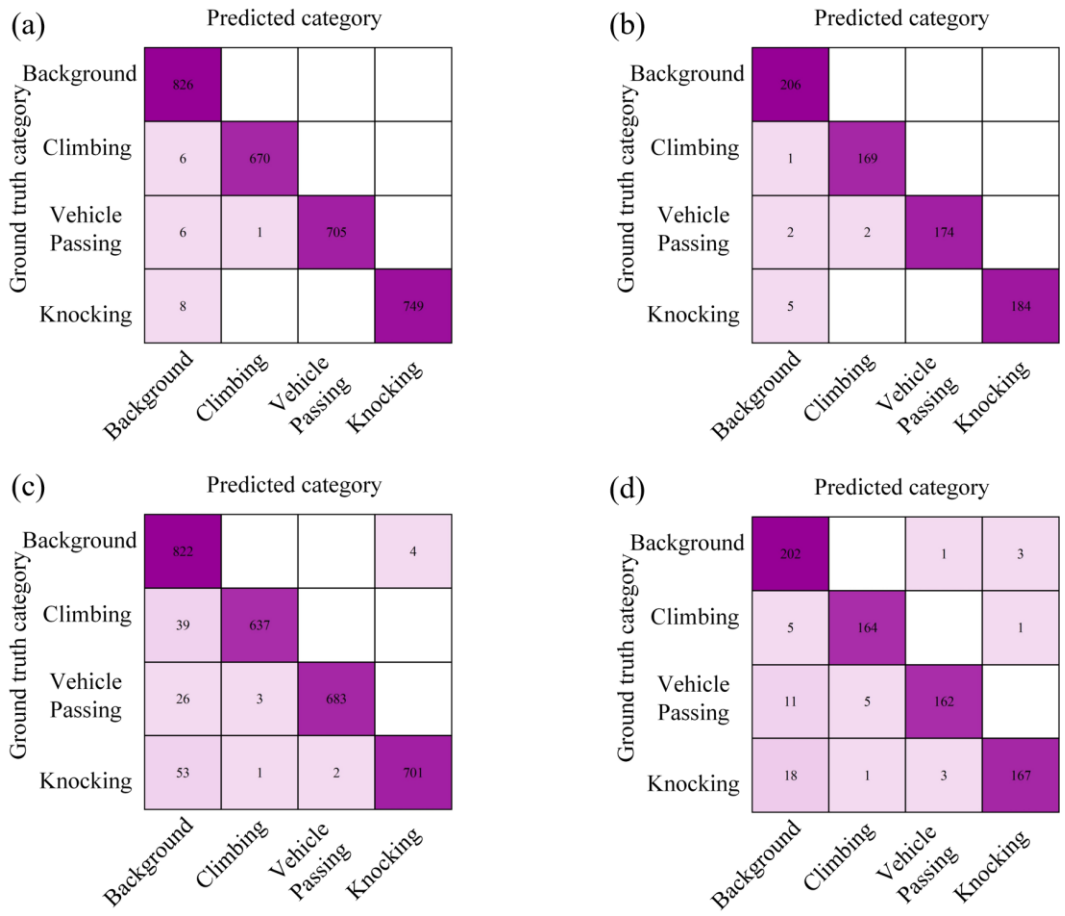

Fig. S9. The confusion matrix for the DAS classification task, input size = 128 ×128: (a) Confusion matrix for the Electrical CNN during training; (b) Confusion matrix for the Electrical CNN during testing; (c) Confusion matrix for the TWM-PNNA during training; (d) Confusion matrix for the TWM-PNNA during testing.

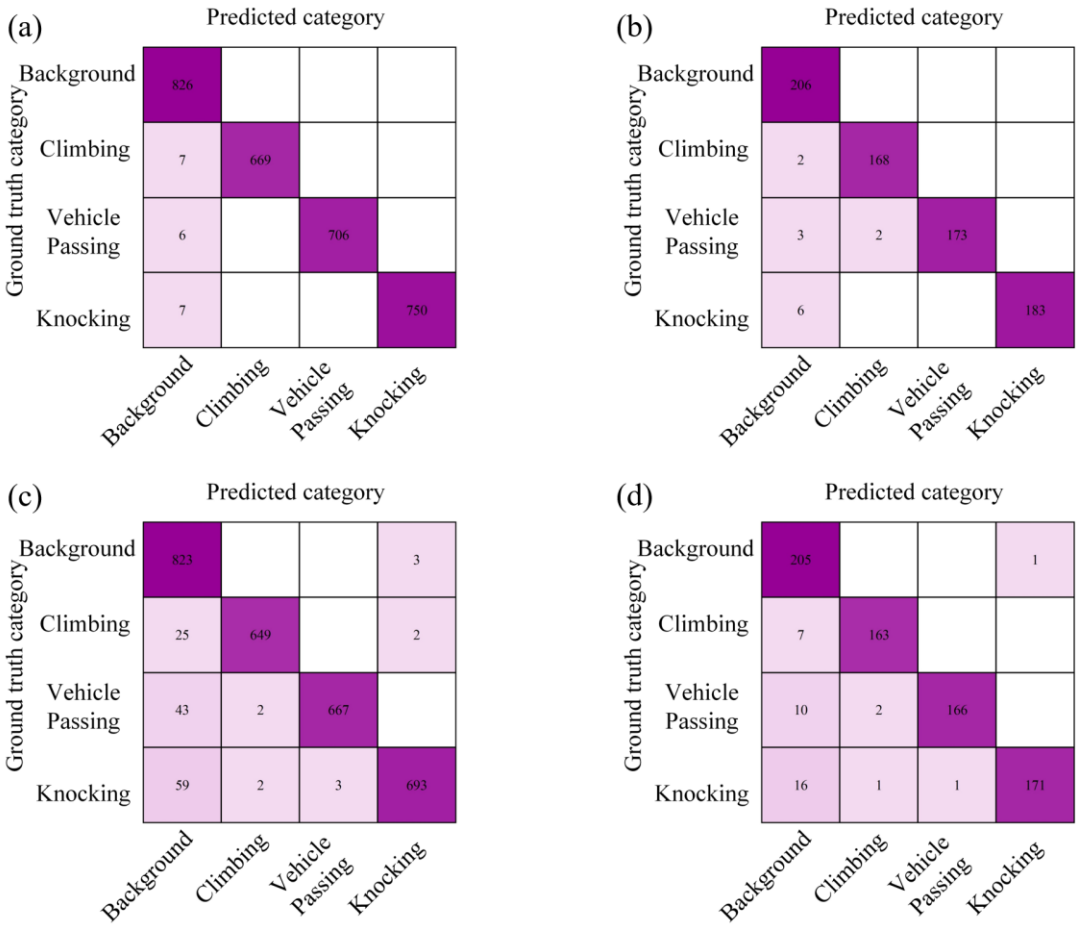

Fig. S10. The confusion matrix for the DAS classification task, input size = 64 ×64: (a) Confusion matrix for the Electrical CNN during training; (b) Confusion matrix for the Electrical CNN during testing; (c) Confusion matrix for the TWM-PNNA during training; (d) Confusion matrix for the TWM-PNNA during testing.

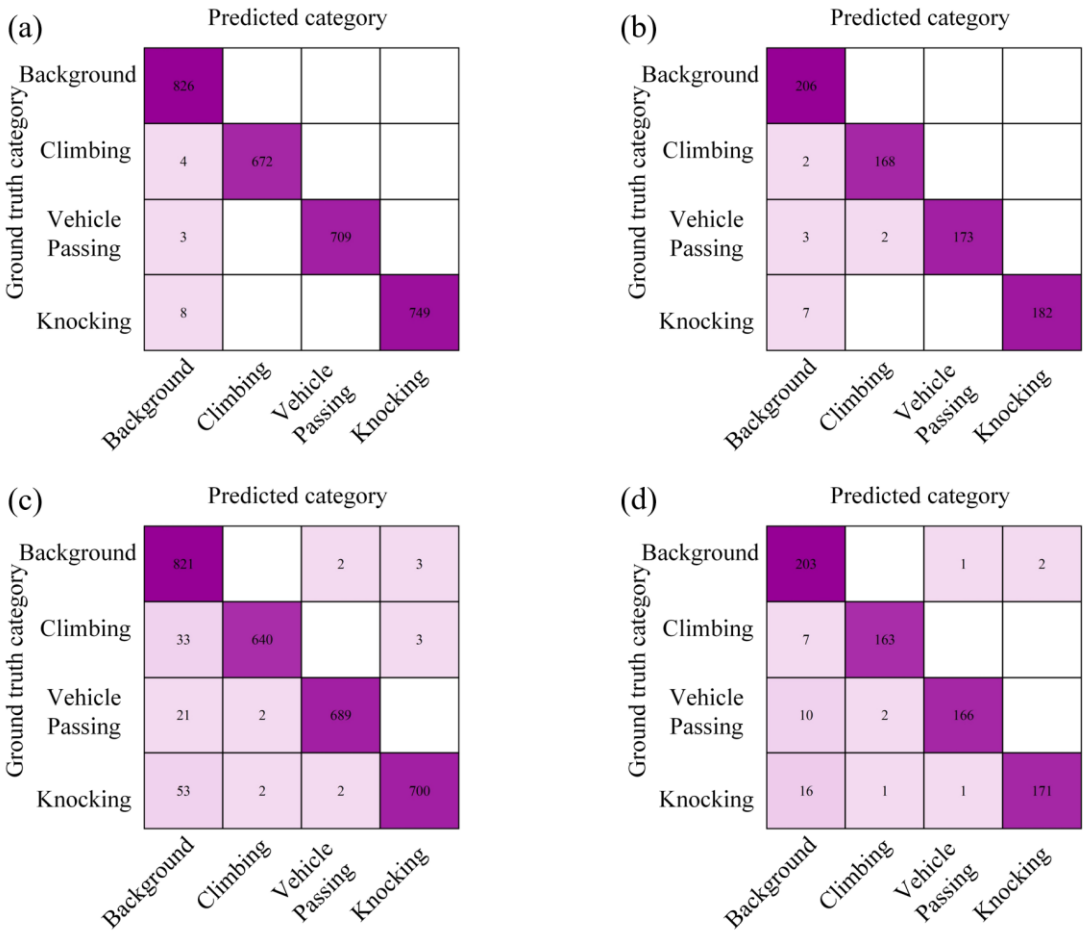

Fig. S11. The confusion matrix for the DAS classification task, input size = 36×36: (a) Confusion matrix for the Electrical CNN during training; (b) Confusion matrix for the Electrical CNN during testing; (c) Confusion matrix for the TWM-PNNA during training; (d) Confusion matrix for the TWM-PNNA during testing.

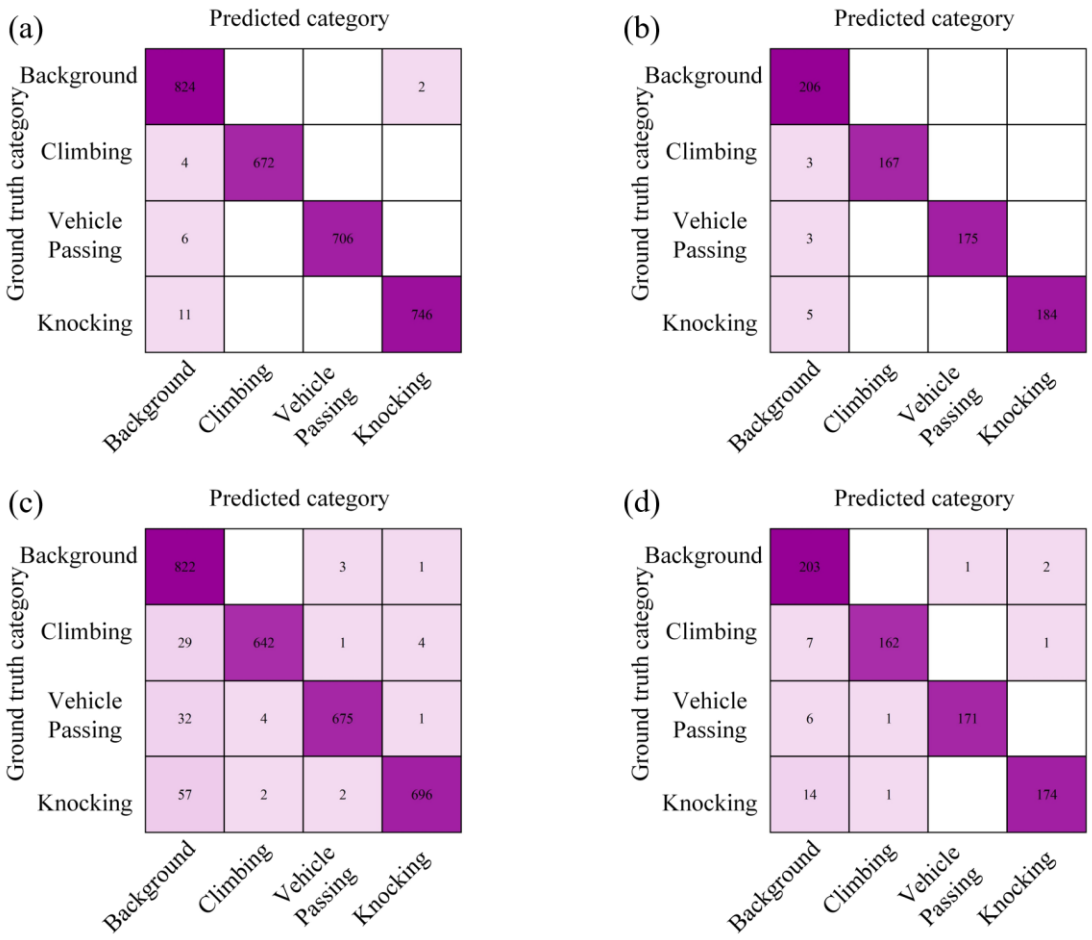

Fig. S12. The confusion matrix for the DAS classification task, input size = 32 ×32: (a) Confusion matrix for the Electrical CNN during training; (b) Confusion matrix for the Electrical CNN during testing; (c) Confusion matrix for the TWM-PNNA during training; (d) Confusion matrix for the TWM-PNNA during testing.

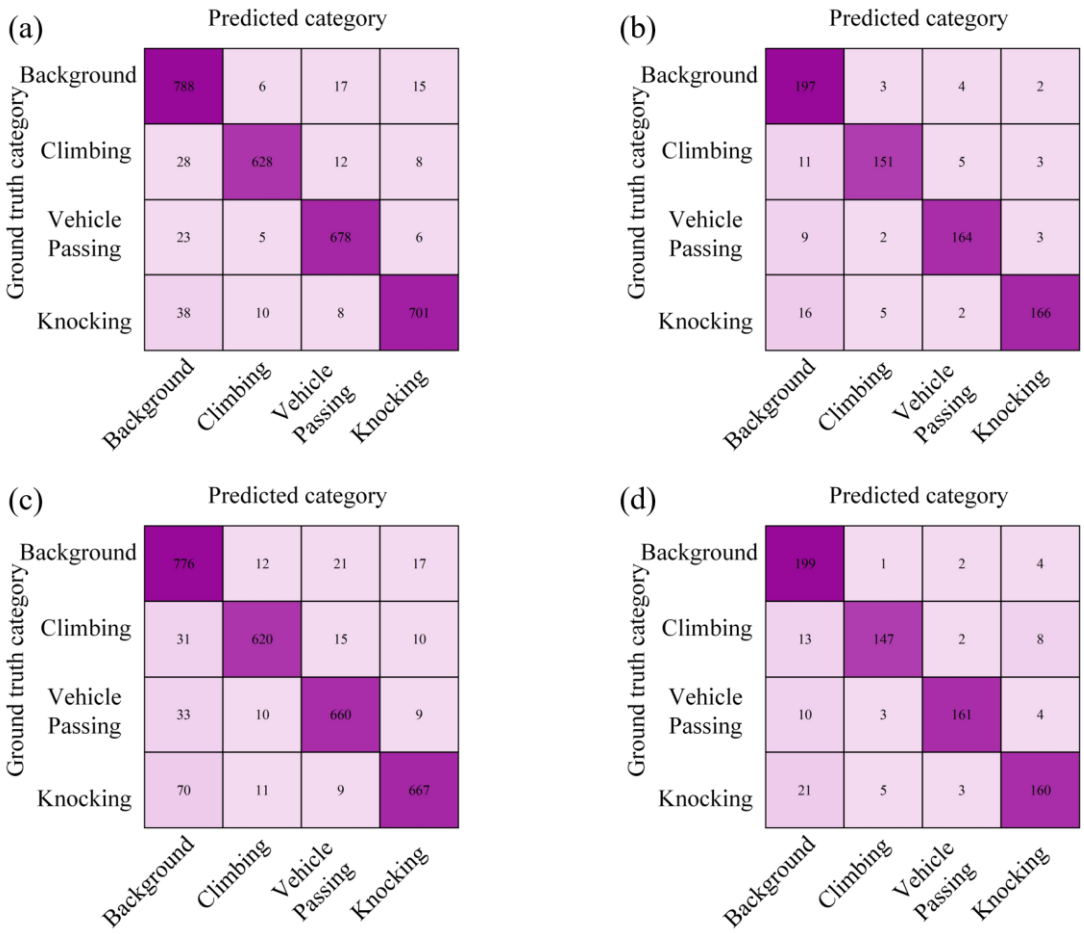

Fig. S13. The confusion matrix for the DAS classification task, input size = 16 ×16: (a) Confusion matrix for the Electrical CNN during training; (b) Confusion matrix for the Electrical CNN during testing; (c) Confusion matrix for the TWM-PNNA during training; (d) Confusion matrix for the TWM-PNNA during testing.

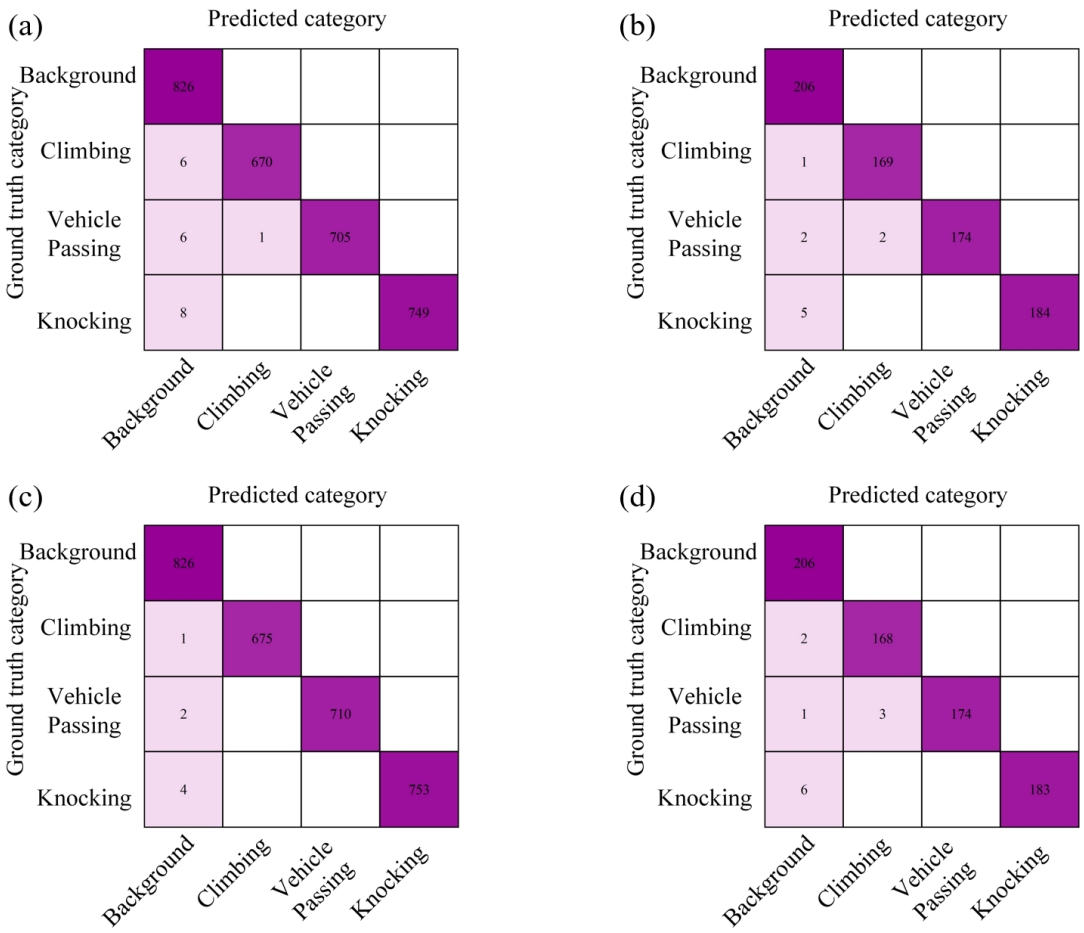

Fig. S14. The confusion matrix for the DAS classification task, input size = 128 ×128. (a) Confusion matrix for the Electrical CNN during training, binary;(b) Confusion matrix for the Electrical CNN during testing, binary;(c) Confusion matrix for the Electrical CNN during training, non-binary;(d) Confusion matrix for the Electrical CNN during testing, non-binary.

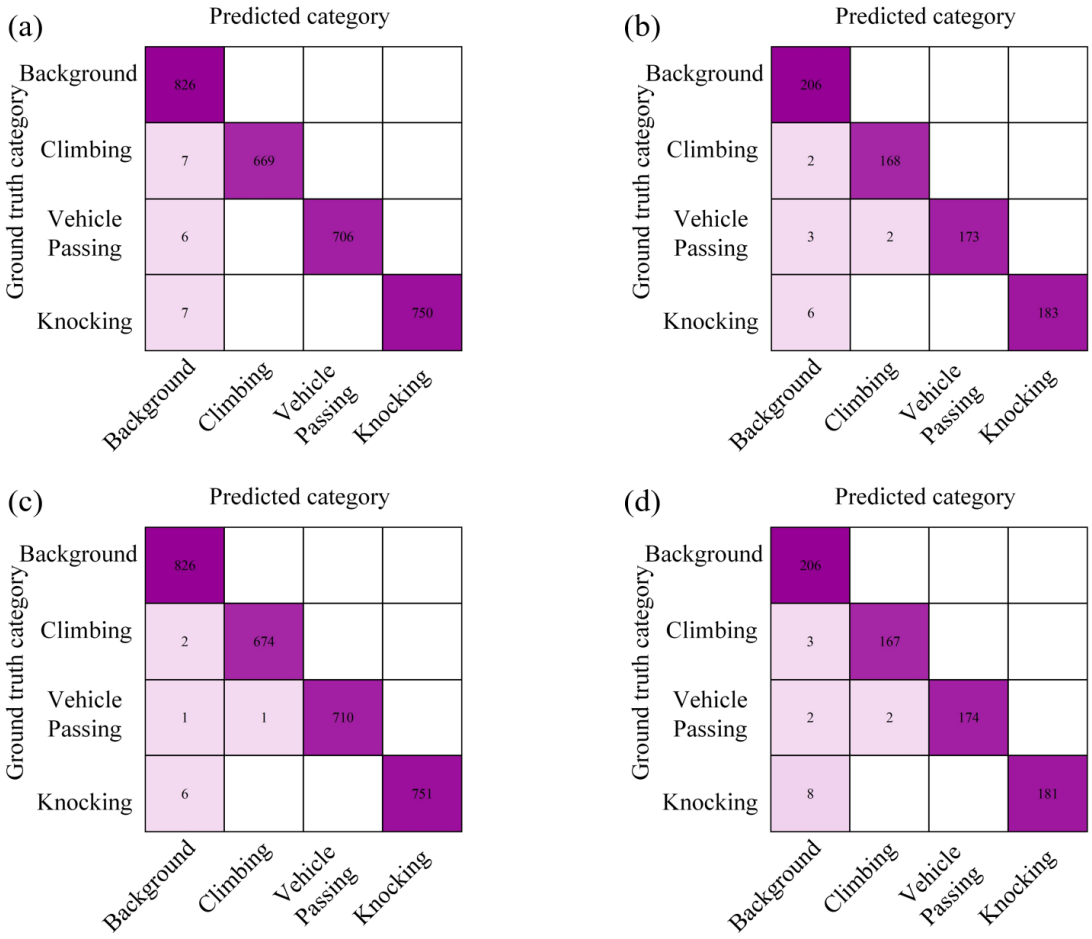

Fig. S15. The confusion matrix for the DAS classification task, input size = 64 ×64. (a) Confusion matrix for the Electrical CNN during training, binary;(b) Confusion matrix for the Electrical CNN during testing, binary;(c) Confusion matrix for the Electrical CNN during training, non-binary;(d) Confusion matrix for the Electrical CNN during testing, non-binary.

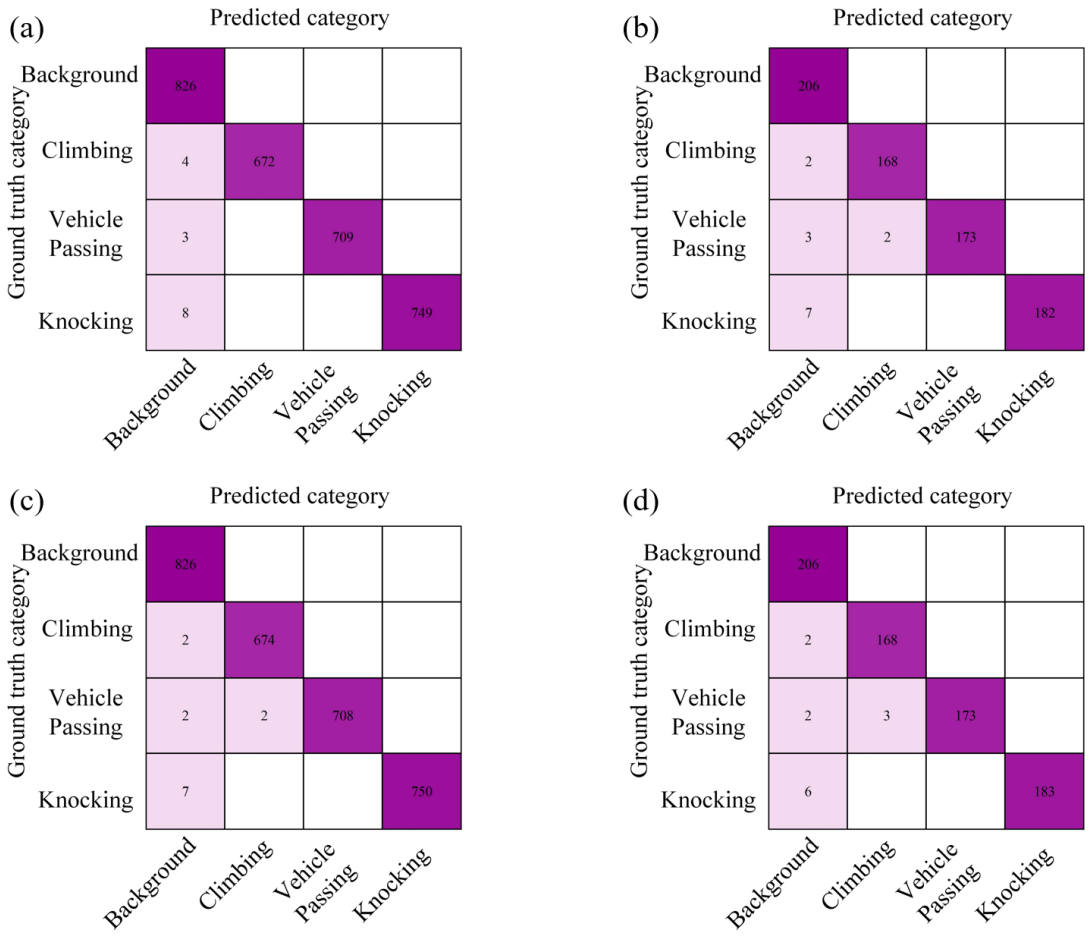

Fig. S16. The confusion matrix for the DAS classification task, input size = 36 ×36. (a) Confusion matrix for the Electrical CNN during training, binary;(b) Confusion matrix for the Electrical CNN during testing, binary;(c) Confusion matrix for the Electrical CNN during training, non-binary;(d) Confusion matrix for the Electrical CNN during testing, non-binary.

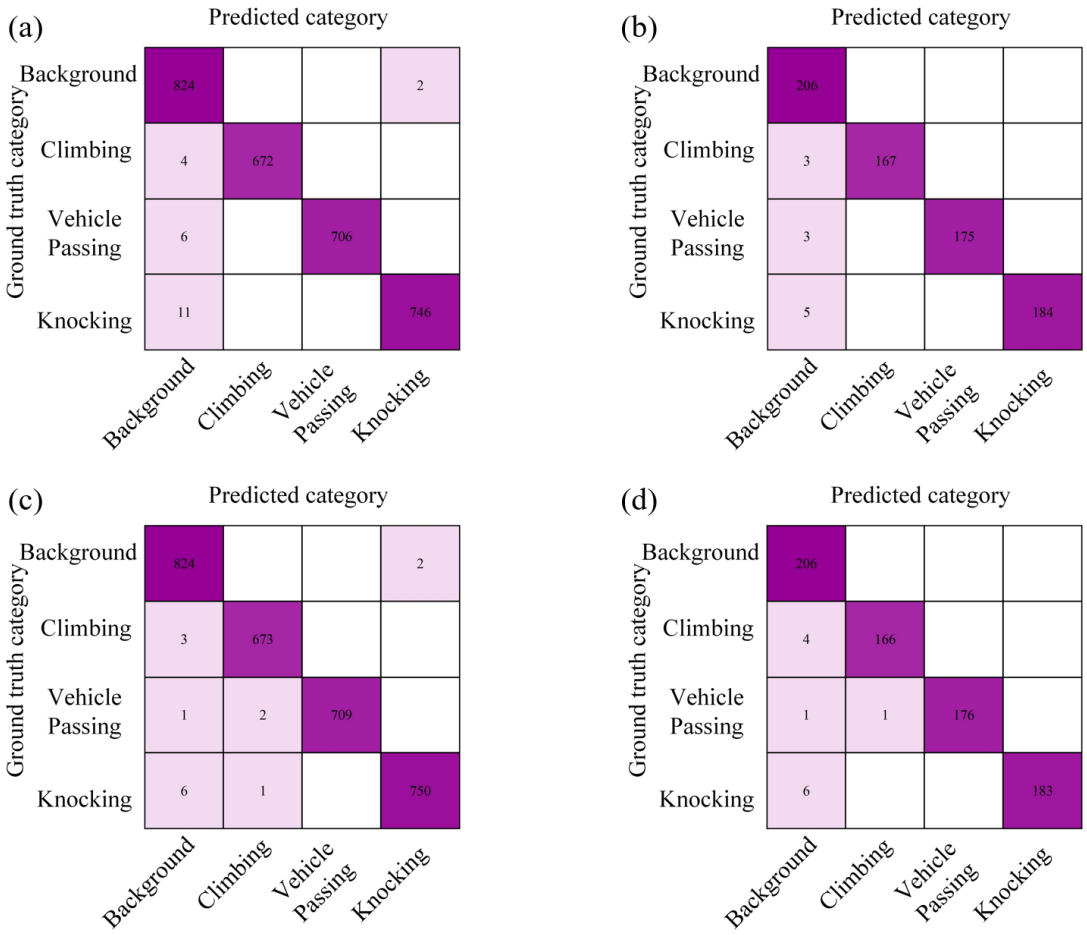

Fig. S17. The confusion matrix for the DAS classification task, input size = 32 ×32. (a) Confusion matrix for the Electrical CNN during training, binary;(b) Confusion matrix for the Electrical CNN during testing, binary;(c) Confusion matrix for the Electrical CNN during training, non-binary;(d) Confusion matrix for the Electrical CNN during testing, non-binary.

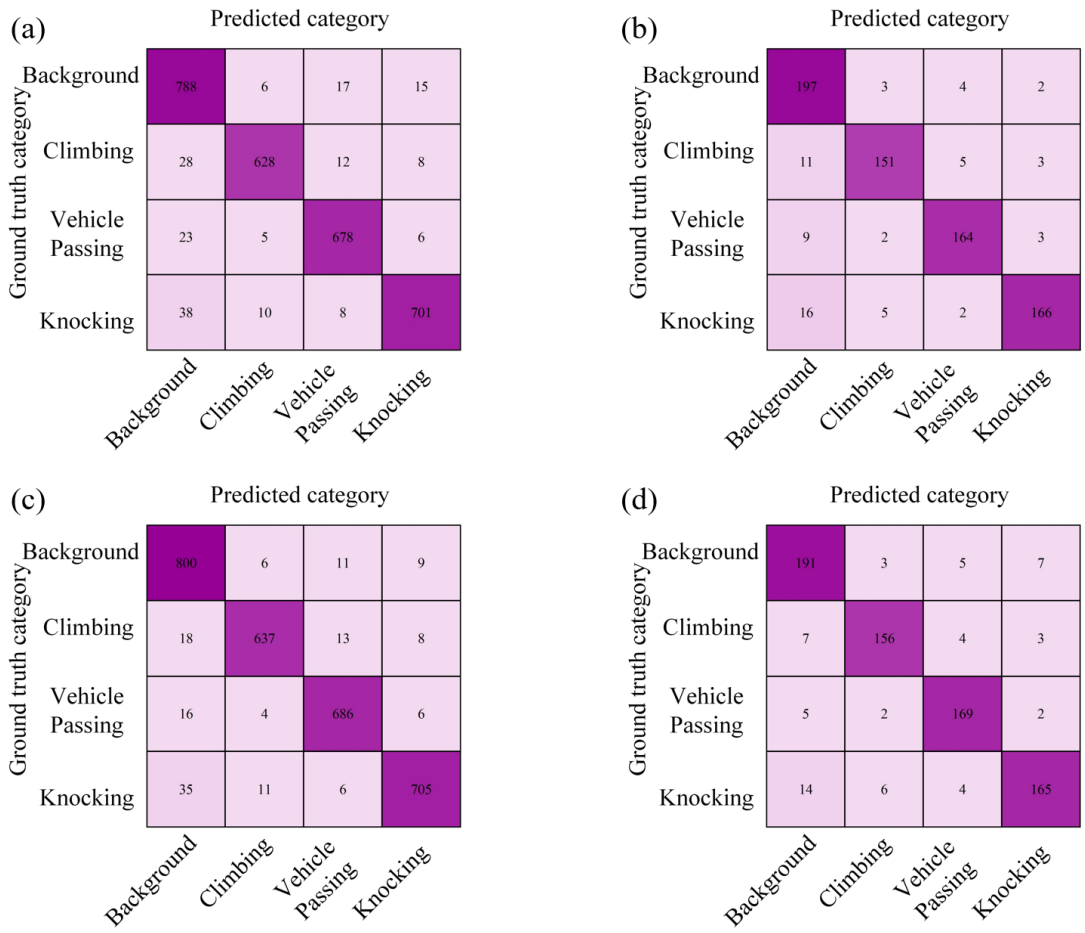

Fig. S18. The confusion matrix for the DAS classification task, input size = 16 ×16. (a) Confusion matrix for the Electrical CNN during training, binary;(b) Confusion matrix for the Electrical CNN during testing, binary;(c) Confusion matrix for the Electrical CNN during training, non-binary;(d) Confusion matrix for the Electrical CNN during testing, non-binary.

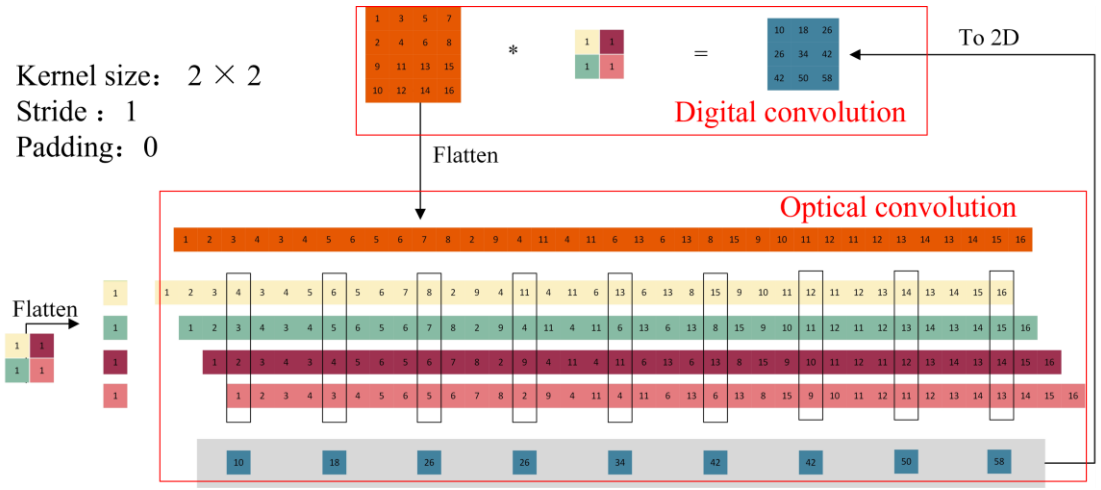

Fig. S19. Two-dimensional data is unfolded according to the convolution rules.

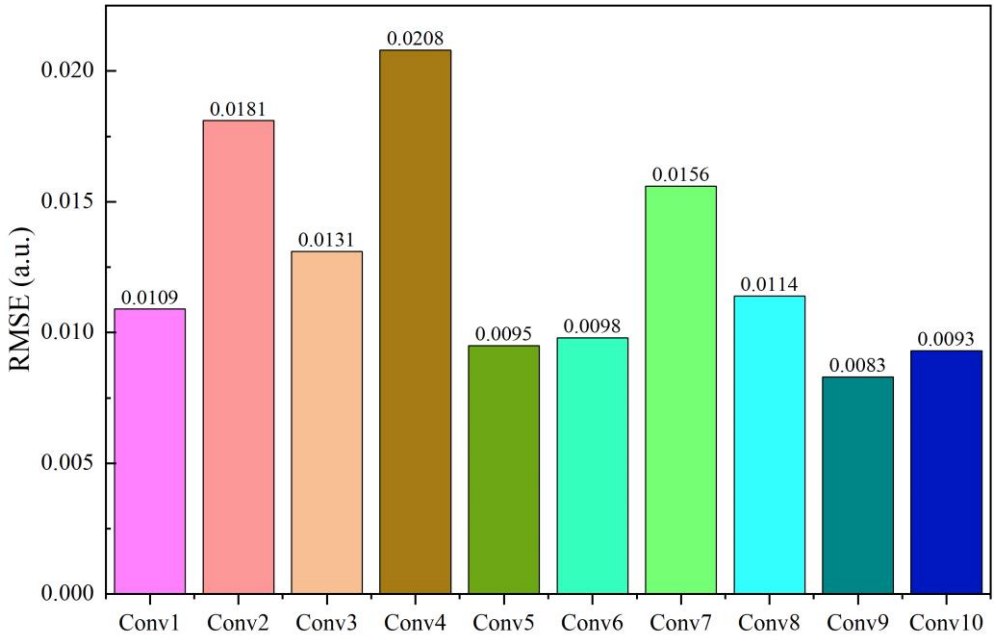

Fig. S20. The RMSE between the TWM-PNNA and electronic computing feature maps.

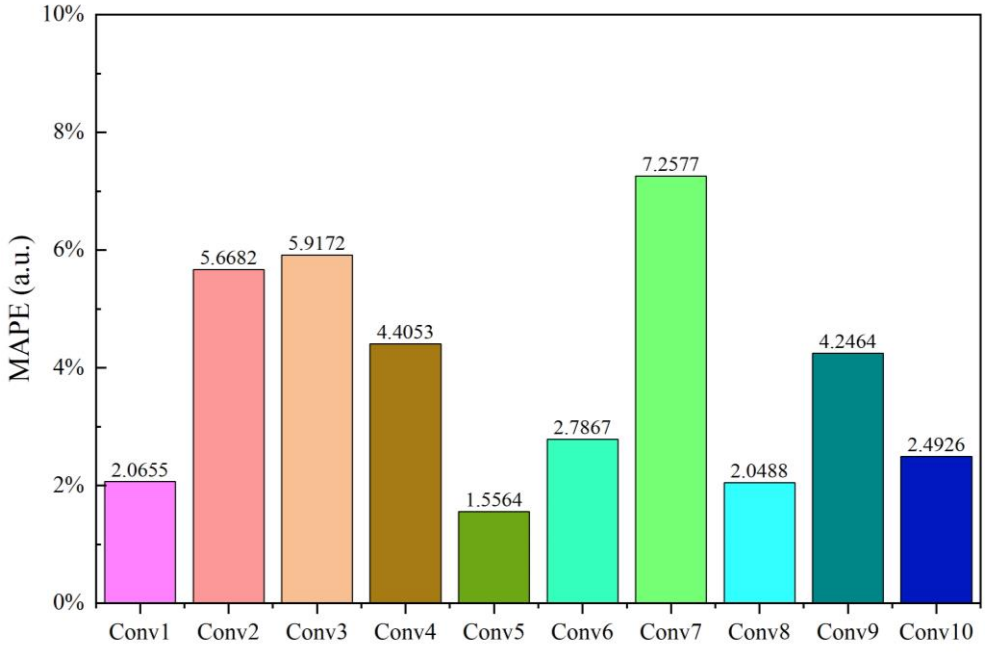

Fig. S21. The MAPE between the TWM-PNNA and electronic computing feature maps.

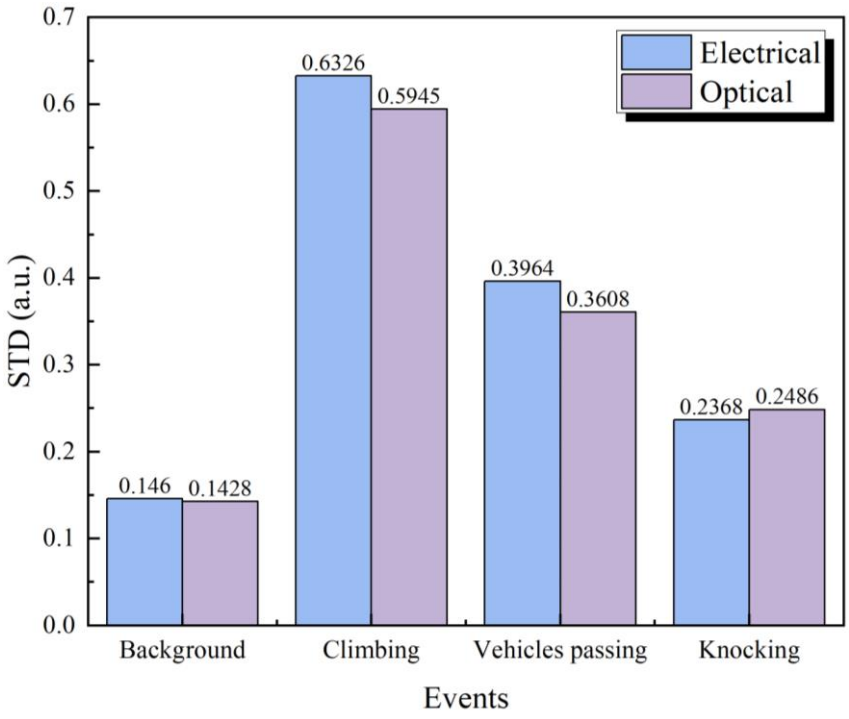

Fig. S22. The STD between different events in TWM-PNNA and electronic computing.